Switch type PANI/ZnO core-shell microwire heterojunction for UV photodetection

Yihan Chen[a], Longxing Su[a,b,*], Mingming Jiang[c], Xiaosheng Fang[a,*]

[a] *Department of Materials Science, Fudan University, Shanghai 200433, China*
[b] *Department of Physical Science and Technology, ShanghaiTech University, Shanghai 201210, China*
[c] *College of Science, Nanjing University of Aeronautics and Astronautics, Nanjing 211106, China*

ABSTRACT

In this study, single crystal ZnO microwires (MW) with size of $\sim$5.4 mm $\times$ 30 μm are prepared through a chemical vapor deposition technique at high temperature (1200 °C). Subsequently, p-type conducting polyaniline (PANI) polymers with different conductivities are densely coated on part of the ZnO MW to construct organic/inorganic core-shell heterojunction photodetectors. The hetero-diodes reach an extremely high rectification ratio (I_{+3V}/I_{-3V}) of 749230, and a maximum rejection ratio (I_{350nm}/I_{dark}) of 3556 (at -3 V), indicating great potential as rectified switches. All the heterojunction devices exhibit strong response to ultraviolet (UV) radiation with high response speed. Moreover, the obvious photovoltaic behavior can also be obtained, allowing the device to operate as an independent and stable unit without externally supplied power. Under 0 V bias voltage, the self-powered photodetector shows a maximum responsivity of 0.56 mA W^{-1} and a rapid response speed of 0.11 ms/1.45 ms (rise time/decay time). Finally, a finite difference time domain (FDTD) simulation is performed to further demonstrate the interaction mechanism between the incident light field and the hexagonal cavity, which strongly supports the enhancement of the light absorption in whispering-gallery-mode resonator.

© 2021 Published by Elsevier Ltd on behalf of Chinese Society for Metals.

Introduction

Owing to the superior electron transport rate in specific direction, non-linear optical effect and self-confinement resonant cavity, low dimensional semiconductors with micro/nano structures have attracted great attention in optoelectronic field including light emitting diodes (LEDs), laser diodes (LDs), photodetectors (PDs), etc[1-8]. These devices are the key components of display, illumination, optical fiber communication, and imaging, which greatly promote the development of fundamental science and practical applications. Compared with the conventional bulk crystal or thin film counterparts, micro/nano structures with size effects and flexibility open a new window to the high performance optoelectronic devices[9-12]. To date, both bottom-up and top-down fabrication processes are utilized to prepare corresponding micro/nano structures including micro/nano wires[13-15], sheets[16,17], walls[18-20], rings[21-23], etc. The top-down craft can be easily integrated with the large-scaled Si-based complementary metal oxide semiconductor (CMOS) technology, while the bottom-up technique shows the advantages of low cost, flexibility and portability.

ZnO, as a wide direct bandgap ($\sim$3.37 eV) semiconductor with a large exciton binding energy of 60 meV, has been regarded as the next-generation optoelectronic material to fabricate high-efficiency excitonic laser devices and UV photodetectors[24-27]. Compared with its counterparts, e.g., GaN, the lower growth temperature and much larger element abundance make ZnO a promising competitor. However, unlike n-ZnO, which is accessible for its intrinsic donor defects or easy doping of Ga[28] or Al[29], p-ZnO is rather difficult to achieve owing to the low solid concentration, unstable and deep energy level properties of acceptors[30]. Thus, to construct p-n heterojunctions with n-ZnO, other inorganic materials such as p-Si[31], p-GaN[32, 33], p-NiO[34, 35], p-Cu$_2$O[36], p-MnWO$_4$[37] are employed as the alternated p-type semiconductors. In these cases, the staggered (type-II) band alignment between hetero-materials yields a photovoltaic effect, which significantly facilitates the separation of photogenerated electron-hole pairs and contributes to the self-powered performance. Besides, organic materials like polyaniline (PANI) are also considered as potential candidates to hybrid heterojunction with n-ZnO due to the features of easy processing, low cost, high flexibility, high stability and conjugated π-electrons in the polymer backbone. PANI is an intrinsic p-type conducting polymer with adjustable hole mobility from 10^{-6} to 3.36 cm^2 V^{-1} s^{-1}, which is determined by the dopant types and oxidation

state[38, 39]. As a result, the electrical conductivity can be modulated over many orders of magnitudes. Chen et al.[40] prepared an all-solid-state polyaniline/MgZnO bilayer through a simple transfer method. The device could function as a high-sensitivity self-powered solar-blind photodetector with a UV/Visible rejection ratio of 10^4. However, the maximum responsivity of the device under 0 V bias voltage was only 160 μA/W, and the response time was relatively long (~0.3 s). Wang et al.[41] further reported a β-Ga_2O_3/PANI core-shell microwire heterojunction for solar-blind photodetector with high responsivity of 21 mA/W (at 0 V) and extremely low dark current of 80 fA. In their work, a simple immersion method was employed to prepare the core-shell configuration, strongly indicating the flexible and facile device integration of the p-type polymer PANI with inorganic semiconductors.

In this work, PANI/ZnO core-shell microwire heterojunctions were fabricated through a simple electrochemical deposition method. The conductivities of PANI layers are modulated by adjusting the dose of aniline precursors during the synthesis process. A clear interface of ZnO/PANI and the densely coated morphology were observed in the SEM measurement. The rectification ratio (I_{+3V}/I_{-3V}) of heterojunction devices reached an extremely high value of 749230, indicating its great potential as a switch type diode. Besides, the devices showed significant response to UV light along with rapid response at a scale of microseconds to milliseconds. Moreover, the PANI/ZnO core-shell microwire heterojunction with 35 μL dose of aniline revealed superior self-powered behavior. Finally, a FDTD simulation was utilized to analyze the light confinement inside the organic/inorganic core-shell structure, further explaining the working mechanism of the photodetectors.

Experimental

Material synthesis

The ZnO MWs were synthesized by a simple carbothermal reduction method. The growth temperature was steadied at 1200 °C, providing a hypoxic growth environment for high-quality ZnO MWs. The precursors, a mixture of high-purity ZnO and graphite C powders with a weight ratio of 1:1, were loaded with a corundum boat and placed in the center of the furnace. During the microwire growth process, a constant flow of argon (Ar: 99.99%, 200 sccm) served as the protective and carrier gas. High purity oxygen (O_2: 99.99%, 20 sccm) was adopted as the reaction oxygen source. A mass of individual ZnO MWs can grow onto the Si substrate (located at the downstream of the ZnO/C powders) by a carbothermal method from the precursor mixture. Schematic synthesis procedure was provided in Fig. S1 (in Supplementary Information). The PANI samples were synthesized through a solution method. A certain dose of aniline (25, 30, 35, 40 μL) was added to 20 mL of 1 M H_2SO_4 aqueous solution with glass substrates (1 cm × 1 cm) submerged in it and then stirred till complete dispersion at 0 °C. Another 20 mL of 1 M H_2SO_4 cold aqueous solution containing potassium persulfate (75 mg) was rapidly added and stirred for 30 s. The polymerization process was carried out at 0 °C for 24 h and took place on the surfaces of the glass substrates to form continuous PANI films, the thickness of which is in the order of hundred nanometers. The glass substrates completely wrapped with PANI films were the obtained samples, which afterwards were dried at 80 °C for 12 h. The PANI samples with different aniline (AN, 25, 30, 35, 40 μL) doses are denoted as PANI #1, #2, #3, and #4.

Characterization

The morphologies of ZnO MW and PANI/ZnO MW photodetector were characterized by field-emission SEM (FESEM) (Zeiss Sigma).

The crystal structure of ZnO MW was identified by X-ray diffraction with Cu K$_\alpha$ radiation (λ = 1.5419 Å) (Bruker, D8-Advance) and the chemical bonding characteristics of PANI were studied by a Raman spectroscope using 532 nm argon ion laser (Spex 403). The absorption spectra of PANI were characterized by using a UV-Vis-NIR scanning spectrophotometer (Hitachi, U-3900H) with an integrating sphere attachment. The PANI film thickness was measured by AFM (Bruker, Dimension Edge).

Device fabrication and measurement

One single ZnO MW was made contact with a prepared PANI sample and the In electrodes were pressed on the ZnO MW end and the PANI surface, respectively. The PANI was electroplated onto the ZnO MW at -3 V bias, forming a densely coated PANI/ZnO MW core-shell structure (the detailed process is described in Fig. S2). The core-shell devices with different aniline (AN, 25, 30, 35, 40 μL) doses are denoted as device #1, #2, #3, and #4. The photoelectric performance of PANI-ZnO MW photodetectors was analyzed with a Xe lamp, monochromator and a program-controlled semiconductor characterization system (Keithley 4200 and 4200 remote preamps). The transient response performance of the device was evaluated with an oscilloscope (Tektronix MSO/DPO5000) and a pulsed YAG:Nd laser (Continuum Electro-Optics, MINILITE II, 355 nm, 10 Hz). The optical power density was measured with a power meter (OPHIR photonics, NOVA II).

Results and discussion

Fig. 1(a) presents the atomic arrangement along c-direction of wurtzite ZnO. The chemical bond lengths of the Zn–O parallel to c-direction are ~2.001 Å and the other Zn–O bond lengths are ~1.992 Å according to the previous reports[42]. Fig. 1(b) is the schematic structure of the as-prepared high-quality ZnO MW. In our work, the ZnO MW reveals a c-direction growth preference and a high aspect ratio. Fig. 1(c) shows the chemical molecular structure unit of conducting polymer PANI, containing a reduced unit (a benzene structure composed of a benzene ring and its bridged NH atoms) and an oxidized unit (a quinone structure composed of a quinone ring and its bridged N atom). Generally, the conductivity of PANI can be adjusted through controlling the ratio of quinone rings and benzene rings. Fig. 1(d) illustrates the measurement configuration of the hetero-device constructed by the as-prepared ZnO MW (core) and PANI (shell), from which the PANI/ZnO MW heterojunction UV photodetector was irradiated by the monochromatic light from Xe-lamp and the photogenerated electron-hole pairs were simultaneously collected by the semiconductor parameter meter.

Fig. 2(a) exhibits the XRD pattern of one single ZnO MW, from which the two strong peaks locating at ~32° and ~66.57° are observed, which can be ascribed to the (100) and (200) diffraction signals of wurtzite ZnO. The strong intensity and narrow full width at half maximum (FWHM) indicate the excellent crystal quality of the ZnO MW grown at high temperature. The small and wide peak at 22.7° should be ascribed to C (120), which originates from the graphite C powders used for the ZnO microwire growth. The normalized micro-region absorption spectrum of one single ZnO MW is presented in Fig. 2(b). The sharp absorption edge at ~380 nm can be attributed to the near band edge absorption. Oscillating stripes in visible region can also be observed, which originate from the Fabret-Perot interference between two opposite facets of the hexagonal ZnO MW. The room temperature PL spectrum of ZnO MW is also measured and presented in Fig. S3. Obviously, only a strong near band edge UV emission peak centered at ~380 nm with a full width at half maximum of ~10 nm is observed, while no defect-related emissions can be detected. The PL measurement
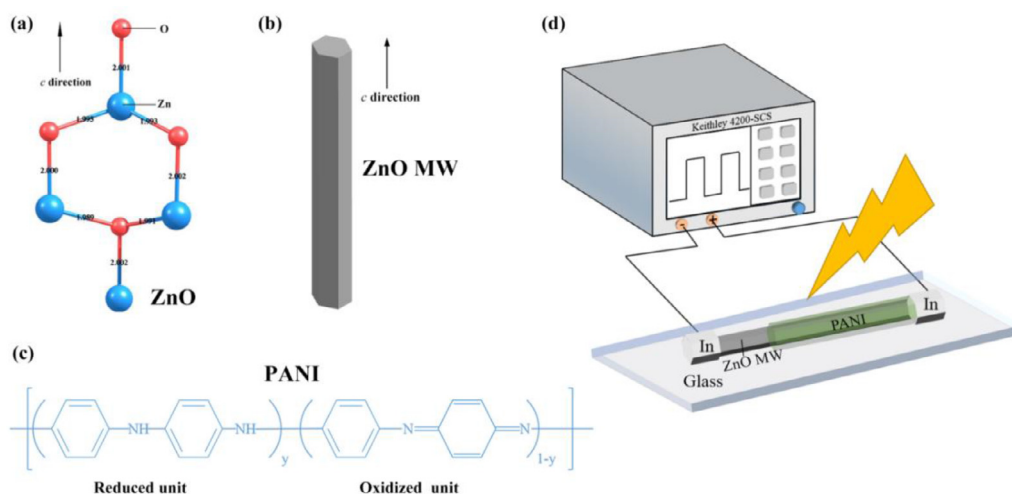
Fig. 1. (a) Schematic atom structure of ZnO; (b) schematic structure of as-grown ZnO MW by CVD; (c) the chemical molecular structure of PANI; (d) measured configuration of PANI/ZnO MW heterojunction UV photodetector.
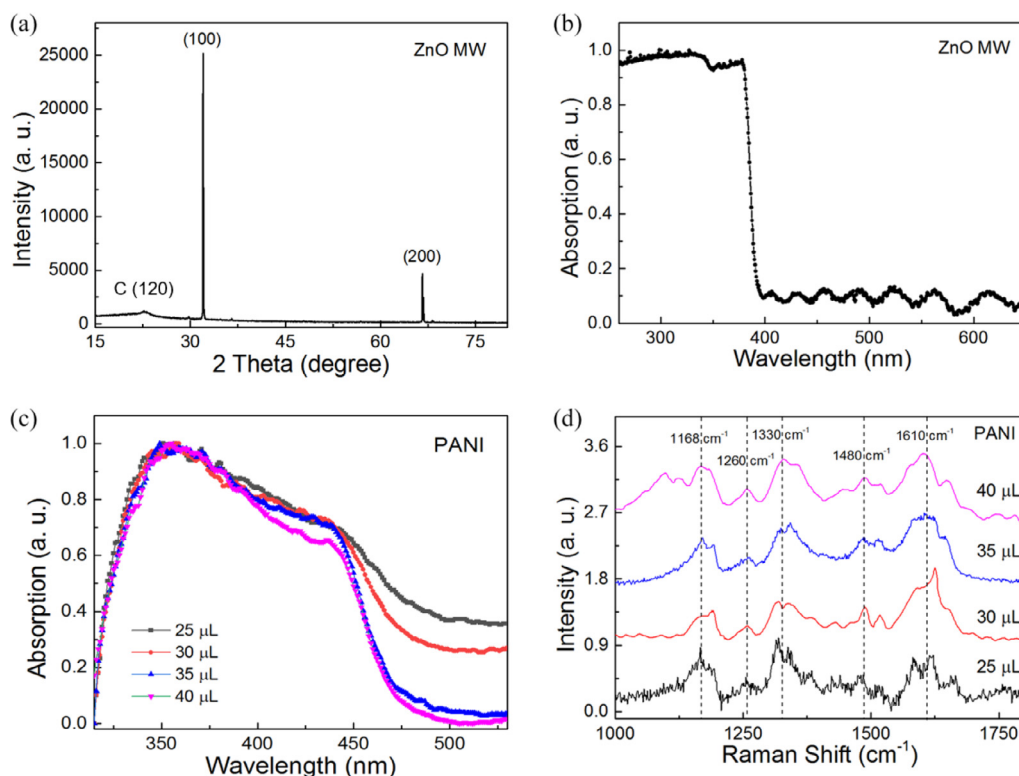

Fig. 2. (a) XRD pattern and (b) normalized absorption spectrum of one single ZnO MW; (c) normalized absorption and (d) Raman spectra of PANI samples with aniline doses of 25 μL, 30 μL, 35 μL and 40 μL.

further demonstrates the high quality of ZnO MW. The normalized absorption spectra of the PANI samples are shown in Fig. 2(c), exhibiting a prominent absorption from blue light to UV region. Raman spectroscopy is performed to further confirm the existence and chemical vibration characteristics of the as-prepared PANI. As indicated in Fig. 2(d), the characteristic peaks of all the PANI samples locate at ~1168 cm^{-1}, 1260 cm^{-1}, 1330 cm^{-1}, 1480 cm^{-1}, and 1610 cm^{-1}, in line with the typical vibration frequencies of PANI as indexed. According to previous reports[40, 41], these peaks can be identified as the vibrations of C-H bonding of the quinoid rings, C-N vibration of the benzene diamine units, C=N vibration of the quinoid nanoprotonated diamine units, C=C vibration of the quinoid rings and C-C stretching of the benzenoid rings, respec-

tively. The Raman spectra also reveal the change in the ratio of quinoid diamine units to benzene diamine units (Q/B) in the four PANI samples through peak separation, which is demonstrated in Fig. S4. As integration calculated, the Q/B of PANI #1, #2, #3, #4 is 1.025, 1.090, 1.175, 1.076, respectively. According to the doping mechanism of PANI, the value of Q/B for the highest conductivity is 1[43]. Thus, the Q/B variation indicates a conductivity increase in PANI from #1 to #3 and a decrease from #3 to #4. Besides, It is worth noting that the Raman spectra also reveal tiny frequency shifts in different PANI samples, which can be ascribed to the fluctuation of corresponding chemical bond strengths.

Fig. 3(a) shows one single ZnO MW on the Si substrate. The length of the ZnO MW can be confirmed as ~5.4 mm. The SEM
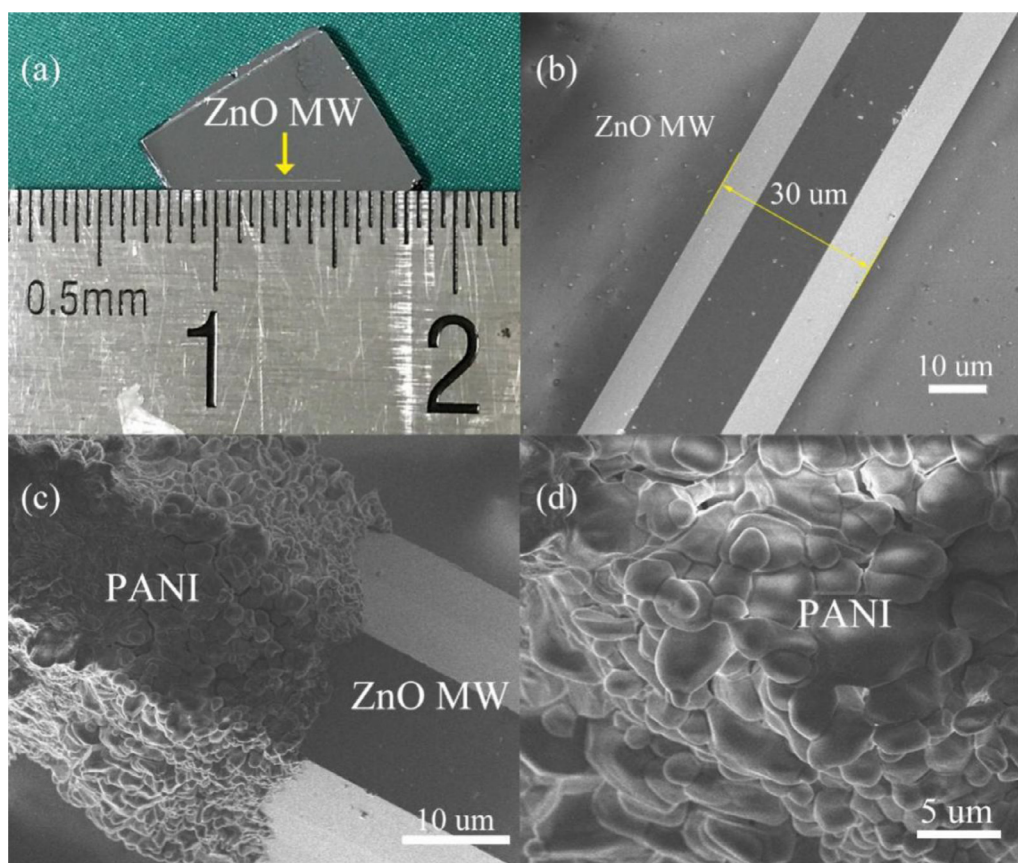
Fig. 3. (a) Optical image of one as-prepared ZnO MW on Si substrate, (b) SEM image of the as-prepared single ZnO MW; (c) SEM image of the PANI/ZnO MW core-shell heterostructure; (d) SEM image of the PANI from the core-shell heterostructure.
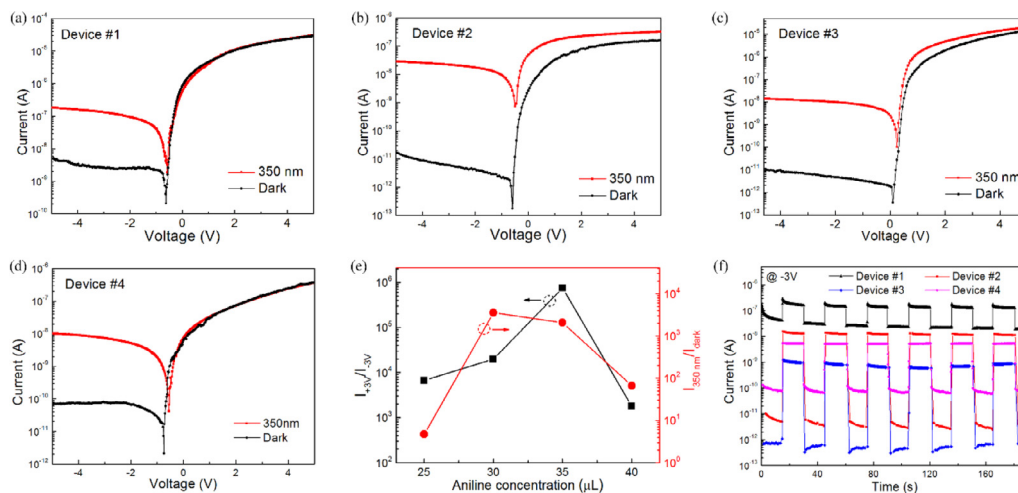

Fig. 4. (a-d) I-V curves of device #1, #2, #3, and #4 under dark and 350 nm light illumination; (e) rectification ratio (I_{+3V}/I_{-3V}) (black line) and rejection ratio ($I_{350\ nm}/I_{dark}$) (red line) of the PANI/ZnO heterojunctions at -3 V as a function of aniline dose; (f) I-T curves of the four devices under a 350 nm light illumination on/off switch at -3 V.

method was employed to further investigate the morphology of the PANI/ZnO MW. As revealed in Fig. 3(b), the width of the ZnO MW is measured as 30 μm and the surface shows extremely smooth property, which is mainly attributed to the high growth temperature. Furthermore, a hexagonal structure can be observed, agreeing well with the XRD result. Fig. 3(c) illustrates the core-shell structure, of which the PANI is tightly and densely coated on part of the ZnO MW and shows a clear boundary from ZnO. The PANI synthesized by solution method exhibits a 3D island-like morphology (Fig. 3(d)).

Fig. 4(a-d) presents the current-voltage (I-V) curves of device #1, #2, #3, and #4 under dark and 350 nm light illumination. The four devices exhibit superior rectification behavior under dark environment, from which the devices are in on-state at positive bias voltage and in off-state at negative bias voltage. Fig. S5(a-e) provides the I-V curves of the pristine ZnO MW and the four PANI samples using indium (In) as electrodes, from which the linear current-voltage relationship can be obtained, indicating the Ohmic contact between In electrodes and the active materials. Therefore, it can be verified that the rectification behaviors of the four
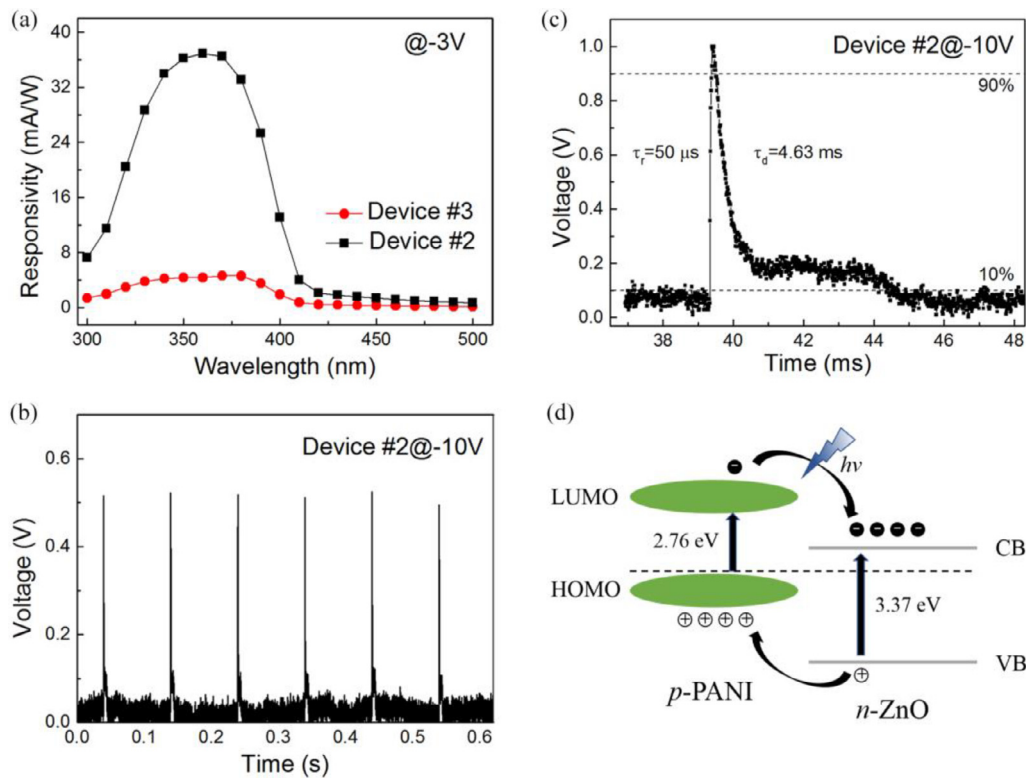
Fig. 5. (a) Responsivities of device #2 and #3 under -3 V bias voltage; (b) 6-cycle transient time-resolved response of device #2 under 355 nm pulse laser illumination at -10 V bias voltage; (c) one single period time-resolved response of device #2 derived from (b); (d) schematic energy band diagram of the PANI/ZnO heterojunction.

devices originate from the PANI/ZnO heterojunctions. All the devices do not show any leakage currents under negative bias voltage, possibly ascribed to the low concentration of leakage channels in the heterojunction. Especially in device #2 and #3, the dark currents are at a scale of picoamperes, indicating the low dark noise. Under 350 nm light illumination, the four devices exhibit significant enhancement in current at negative bias voltages. More importantly, all the light currents at positive bias voltages show limited variations from the dark ones, the light and dark currents of device #1 and #4 at positive bias voltages are even the same. This indicates the suppression of parasitic photoconductivity, which may contribute to a faster response speed. The rectification ratios (I_{+3V}/I_{-3V}) and rejection ratios (I_{350nm}/I_{dark}) of different PANI/ZnO core-shell heterojunctions are summarized in Fig. 4(e). The rectification ratios (I_{+3V}/I_{-3V}) of the four devices are 6614, 19632, 749230, and 1794, much higher than previous reports on PANI/Ga$_2$O$_3$[41], SnO$_2$/CuZnS[44] and ZnO/Ga$_2$O$_3$[45] heterojunctions. Device #3 with a high rectification ratio of 749230 can be further utilized as a well-functioned on/off switch in clipper circuits, clamping circuits, ESD protection, etc[46]. The rejection ratios (I_{350nm}/I_{dark}) in Fig. 4(e) reveal the UV light response capability of the devices at -3 V. The rejection ratios of device #2 and #3 can reach as high as 3556 and 2080, indicating the strong UV response properties of the PANI/ZnO core-shell heterojunctions. Fig. 4(f) presents the current-time (I-T) curves of the four different devices under a 350 nm light illumination on/off switch at -3 V. All the four devices exhibit remarkable photoresponse, superior stability and repeatability in each cycle. Interestingly, the different doses of aniline result in the different conductivities of the four PANI samples (indicated in Fig. S6 and Table S1), contributing to the varied optoelectronic performances. Compared with device #1 and #4, device #2 and #3 reveal much lower dark current and much higher photoresponse under the same condition, thus the responsivity, detectivity and response speeds of which are worth

further investigating, while the less outstanding device #1 and #4 are unconsidered.

The responsivity R_λ is a key parameter to evaluate the photon-electron conversion ability of a photodetector. It can be calculated with the following equation[40,41]:

$$R_\lambda = (I_{ph} - I_d)/P_\lambda S \tag{1}$$

where P_λ is the optical power density, I_{ph} is the photocurrent, I_d is the dark current, and S is the effective illuminated area of the device. Fig. 5(a) shows the spectral responsivities of device #2 and #3 under -3 V bias voltage, both devices reveal prominent response in UV region and the peak responsivities are calculated as 37 mA W^{-1} and 4.6 mA W^{-1} according to Equation (1), the difference mainly owing to the conductivity variation between the PANI of the two devices. The detectivity D*, another key parameter of a photodetector, is introduced to evaluate the response sensitivity to the weak signal. Under the dark current dominated situation, the detectivity D* can be defined as [40,41]:

$$D* = R_\lambda / (2qI_d/S)^{1/2} \tag{2}$$

where q is the elemental charge. According to Equation (2), the maximum detectivity under -3 V of the device #2 and #3 can be calculated as 1.32×10^{12} Jones and 4.05×10^{11} Jones, respectively. The response speed of device #2 under -10 V is also measured using an oscilloscope coupled with a 355 nm pulse laser. Six-cycle time-resolution response is presented in Fig. 5(b). Device #2 shows excellent stability and repeatability even under the strong laser light, further verifying its high performance. From one enlarged time-resolution response cycle shown in Fig. 5(c), the rise time (from 10% to 90% of the maximum response) and decay time (from 90% to 10% of the maximum response) of device #2 are 50 μs and 4.63 ms, respectively, indicating its rapid UV response ability. When the laser is in off-state, the relatively slow decay time and the obvious tail for few milliseconds may be ascribed to the
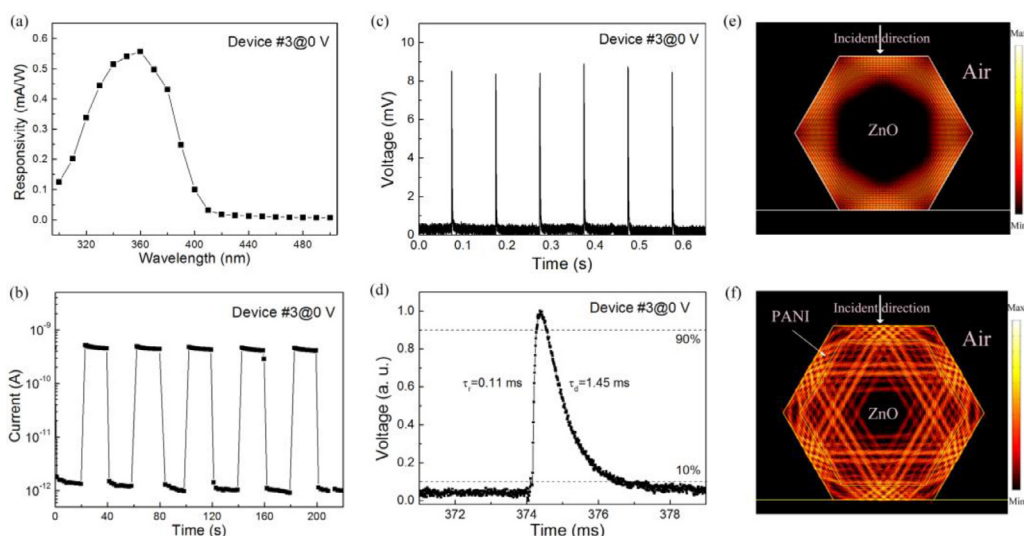
Fig. 6. (a) Responsivities of device #3 under 0 V bias voltage; (b) I-T curve of device #3 under a 350 nm light on/off switch at 0 V, (c) 6-cycle transient time-resolved response of device #3 under 355 nm pulse laser illumination at 0 V bias voltage; (d) one single period time-resolved response of device #3 derived from (c); theoretical simulation of optical field distribution: (e) one single ZnO MW, (f) PANI/ZnO core-shell microwire, the incident light is vertical to one facet of the hexagonal structure.

Table 1
Performance parameter comparison of the reported organic/inorganic heterojunction photodetectors

Photodetector	Bias	Dark current	Rejection ratio	Rectification ratio	Responsivity (mA/W)	Response time	Ref.
PANI NWs/ZnO 2D film	0 V	-	168000	-	8.75×10^{-4}	-	[48]
PANI/β-Ga$_2$O$_3$	0 V	0.08 pA	-	~10000 ($\pm$5 V)	21	0.34 ms / 8.14 ms	[49]
PANI/Se	0V	2 pA	1100	30 ($\pm$5 V)	120	4.5 μs / 42.84 ms	[50]
PANI/MgZnO Thin film	0 V	-	~ 10000	-	0.16	< 0.3 s / < 0.3 s	[40]
PEDOT:PSS/ZnO	0 V	-	-	-	3.5	5.8 ms / 7.3 ms	[51]
Spiro-MeOTAD /ZnO	0 V	-	300	~230 ($\pm$0.52 V)	17	0.2 ms / 0.95 ms	[52]
PANI/ZnO MW	-3 V	0.8 pA	3566	749230 ($\pm$3 V)	37	50 μs / 4.63 ms @ -10 V	This work
PANI/ZnO MW	0 V	-	-	-	0.56	0.11 ms / 1.45 ms	This work

photoconduction effect in the device. The energy band diagram of the PANI/ZnO heterojunction in absence of bias voltage is presented in Fig. 5(d), from which the distinct type-II energy band structure is generated and favorable for the transport of photogenerated carriers. When incident light reaches the interface between the PANI and the ZnO, the built-in potential generated by the p-n heterojunction can quickly separate the photon-excited electron-hole pairs and drive them out of the depletion region, the electrons transporting from the PANI side to the ZnO side with lower energy while the holes moving in the opposite direction.

In the four devices, device #3 reveals superior self-powered performance, allowing its potential in outdoor applications. Under 0 V bias voltage, the maximum responsivity of device #3 is 0.56 mA W^{-1} (Fig. 6(a)) and the detectivity is 3.29×10^{10} Jones, indicating its relatively high collection efficiency of photogenerated carriers and the strong capability for weak optical signal detection even without external supply power. Besides, the on/off state I-T curve under 350 nm light illumination (at 0 V) shown in Fig. 6(b) reveals superior stability and remarkable photoresponse of the self-powered device #3. The on-state current is ~0.45 nA while the off-state current is ~1 pA, contributing to a high on/off ratio of 450. The transient photoresponse of device #3 under 0 V is also measured and presented in Fig. 6(c). Without any externally applied power, the stability can still be maintained. From the detailed

image of one cycle data (Fig. 6(d)), working in self-powered mode, the rise time and decay time of device #3 are 0.11 ms and 1.45 ms, respectively. Compared with recent reports on organic/inorganic based UV photodetectors, our devices show outstanding performance (summarized in Table 1). In order to understand the interaction between incident light field and the core-shell heterojunction, we performed an FDTD simulation in the same size of the device. As indicated in the fundamental mode electric field intensity distribution (Fig. 6(e)), the incident light is vertical to one of the six facets from hexagonal ZnO microwire. According to previous reports[47], the ZnO microwire naturally generates a whispering-gallery resonator cavity (WGM), in which the light wave is reflected by the six facets and can only escape out from the corner, thus strongly confined. In the previously reported ZnO WGM lasing device, the WGM mode significantly improved the lasing performance owing to the resonant effect induced by its six reflection internal facets. While in our photodetector case, the ZnO MW turns the incident light into a stationary wave, subsequently the confinement helps to reduce the loss of light waves from transmission, contributing to the enhancement of photocurrent. As presented in Fig. 6(f), after the PANI coating, the light field distributes in both ZnO microwire and the outer coating PANI layer, while the light waves can still hardly escape from the cavity, indicating the trapping of incident light in the core-shell structure. Considering

the different surface states between the experimental PANI layer (relatively rough) and the theoretical one (smooth), part of the incident light onto the device may be scattered by the PANI layer. However, considering the relatively high transmittance of the PANI layer, most of the incident light cannot escape from the cavity, verifying that the excellent confinement effect is still maintained in the experimental PANI/ZnO core-shell structure.

Conclusion

In conclusion, we successfully prepared the PANI/ZnO core-shell microwire heterojunctions through coating PANI with different conductivities onto the high quality ZnO microwires. The organic/inorganic core-shell structure devices can serve as high performance switch with an extremely high rectification ratio of 749230. Moreover, the hetero-devices show stable and repeatable responses to the UV radiation under 0 V bias voltage and negative bias voltage. At 0 V bias voltage, the maximum responsivity of the devices is 0.56 mA/W, while the response speed remains as fast as 0.11 ms/1.45 ms (rise time/decay time), indicating its potential as a self-powered unit. By using a FDTD simulation, whispering-gallery-mode resonator is proposed to account for the light confinement effect of the hexagonal PANI/ZnO core-shell structure, which contributes to the enhancement of optical absorption. Our investigations may pave a solid path to the future applications of organic/inorganic hybrid photodetectors.

Appendix A. Supporting Material

Supporting Information related to this work can be found in the online version or from the authors.

Conflict of Interest

The authors declare no conflict of interest.

Acknowledgments

Supplementary materials

Supplementary material associated with this article can be found, in the online version, at doi:10.1016/j.jmst.2021.07.031.

References

[1] H.Y. Chen, H. Liu, Z.M. Zhang, K. Hu, X.S. Fang, Adv. Mater. 28 (2016) 403–433.
[2] S. Chu, G.P. Wang, W.H. Zhou, Y.Q. Lin, L. Chernyak, J.Z. Zhao, J.Y. Kong, L. Li, J.J. Ren, J.L. Liu, Nat. Nanotechnol. 6 (2011) 506–510.
[3] X. Dai, S. Zhang, Z.L. Wang, G. Adamo, H. Liu, Y.Z. Huang, C. Couteau, C. Soci, Nano Lett 14 (2014) 2688–2693.
[4] X.S. Fang, L.F. Hu, K.F. Huo, B. Gao, L.J. Zhao, M.Y. Liao, P.K. Chu, Y. Bando, D. Golberg, Adv. Funct. Mater. 21 (2011) 3907–3915.
[5] T. Frost, S. Jahangir, E. Stark, S. Deshpande, A. Hazari, C. Zhao, B.S. Ooi, P. Bhattacharya, Nano Lett 14 (2014) 4535–4541.
[6] L.F. Hu, J. Yan, M.Y. Liao, L.M. Wu, X.S. Fang, Small 7 (2011) 1012–1017.
[7] L.X. Su, W.X. Ouyang, X.S. Fang, . J. Semicond. 42 (2021) 052301.
[8] C. Xie, X.T. Lu, Y. Liang, H.H. Chen, L. Wang, C.Y. Wu, D. Wu, W.H. Yang, L.B. Luo, J. Mater. Sci. Technol. 72 (2021) 189–196.
[9] E.M. Song, C.H. Chiang, R. Li, X. Jin, J.N. Zhao, M. Hill, Y. Xia, L.Z. Li, Y.M. Huang, S.M. Won, K.J. Yu, X. Sheng, H. Fang, M.A. Alam, Y.G. Huang, J. Viventi, J.K. Chang, J.A. Rogers, Proc. Natl. Acad. Sci. U. S. A. 116 (2019) 15398–15406.
[10] R. Yang, R.Z. Li, Y. Cao, Y.Q. Wei, Y.F. Miao, W.L. Tan, X.C. Jiao, H. Chen, L.D. Zhang, Q. Chen, H.T. Zhang, W. Zou, Y.M. Wang, M. Yang, C. Yi, N.N. Wang, F. Gao, C.R. McNeill, T.S. Qin, J.P. Wang, W. Huang, Adv. Mater. 30 (2018) 1804771.
[11] S. Cai, X.J. Xu, W. Yang, J.X. Chen, X.S. Fang, Adv. Mater. 31 (2019) 1808138.
[12] X.J. Xu, J.X. Chen, S. Cai, Z.H. Long, Y. Zhang, L.X. Su, S.S. He, C.Q. Tang, P. Liu, H.S. Peng, X.S. Fang, Adv. Mater. 30 (2018) 1803165.
[13] M.E. Reimer, G. Bulgarini, N. Akopian, M. Hocevar, M.B. Bavinck, M.A. Verheijen, E.P.A.M. Bakkers, L.P. Kouwenhoven, V. Zwiller, Nat. Commun. 3 (2012) 737.
[14] A.M. Leach, M. McDowell, K. Gall, Adv. Funct. Mater. 17 (2007) 43–53.
[15] Y.G. Sun, J.A. Rogers, Nano Lett 4 (2004) 1953–1959.
[16] Y.J. Gong, S.B. Yang, L. Zhan, L.L. Ma, R. Vajtai, P.M. Ajayan, Adv. Funct. Mater. 24 (2014) 125–130.
[17] L.B. Tang, X.M. Li, R.B. Ji, K.S. Teng, G. Tai, J. Ye, C.S. Wei, S.P. Lau, J. Mater. Chem. 22 (2012) 5676–5683.
[18] H.T. Ng, J. Li, M.K. Smith, P. Nguyen, A. Cassell, J. Han, M. Meyyappan, Science 300 (2003) 1249.
[19] Y.J. Hong, H.S. Jung, J. Yoo, Y.J. Kim, C.H. Lee, M. Kim, G.C. Yi, Adv. Mater. 21 (2009) 222.
[20] J.Y. Xu, E. Oksenberg, R. Popovitz-Biro, K. Rechav, E. Joselevich, J. Am. Chem. Soc. 139 (2017) 15958–15967.
[21] P. Chen, S.J. Chua, Y.D. Wang, M.D. Sander, C.G. Fonstad, Appl. Phys. Lett. 87 (2005) 143111.
[22] O.K. Zahr, A.S. Blum, Nano Lett 12 (2012) 629–633.
[23] W. Bogaerts, P. De Heyn, T. Van Vaerenbergh, K. De Vos, S.K. Selvaraja, T. Claes, P. Dumon, P. Bienstman, D. Van Thourhout, R. Baets, Laser Photonics Rev. 6 (2012) 47–73.
[24] D.M. Bagnall, Y.F. Chen, Z. Zhu, T. Yao, S. Koyama, M.Y. Shen, T. Goto, Appl. Phys. Lett. 70 (1997) 2230–2232.
[25] Z.K. Tang, G.K.L. Wong, P. Yu, M. Kawasaki, A. Ohtomo, H. Koinuma, Y. Segawa, Appl. Phys. Lett. 72 (1998) 3270–3272.
[26] K.W. Liu, M. Sakurai, M. Aono, Sensors 10 (2010) 8604–8634.
[27] C. Soci, A. Zhang, B. Xiang, S.A. Dayeh, D.P.R. Aplin, J. Park, X.Y. Bao, Y.H. Lo, D. Wang, Nano Lett 7 (2007) 1003–1009.
[28] M.M. Jiang, G.H. He, H.Y. Chen, Z.Z. Zhang, L.X. Zheng, C.X. Shan, D.Z. Shen, X.S. Fang, Small 13 (2017) 1604034.
[29] F. Maldonado, A. Stashans, J. Phys. Chem. Solids 71 (2010) 784–787.
[30] C.H. Park, S.B. Zhang, S.H. Wei, Phys. Rev. B 66 (2002) 073202.
[31] I.S. Jeong, J.H. Kim, S. Im, Appl. Phys. Lett. 83 (2003) 2946–2948.
[32] W.I. Park, G.C. Yi, Adv. Mater. 16 (2004) 87–90.
[33] L.X. Su, Q.L. Zhang, T.Z. Wu, M.M. Chen, Y.Q. Su, Y. Zhu, R. Xiang, X.C. Gui, Z.K. Tang, Appl. Phys. Lett. 105 (2014) 072106.
[34] H. Ohta, M. Hirano, K. Nakahara, H. Maruta, T. Tanabe, M. Kamiya, T. Kamiya, H. Hosono, Appl. Phys. Lett. 83 (2003) 1029–1031.
[35] M.R. Hasan, T. Xie, S.C. Barron, G.N. Liu, N.V. Nguyen, A. Motayed, M.V. Rao, R. Debnath, APL Mater. 3 (2015) 106101.
[36] M. Izaki, T. Shinagawa, K.T. Mizuno, Y. Ida, M. Inaba, A. Tasaka, J. Phys. D: Appl. Phys. 40 (2007) 3326–3329.
[37] M. Pirhashemi, A. Habibi-Yangjeh, J. Mater. Sci. Technol. 34 (2018) 1891–1901.
[38] S. Bhadra, S. Chattopadhyay, N.K. Singha, D. Khastgir, J. Appl. Polym. Sci. 108 (2008) 57–64.
[39] K.P. Nazeer, S.A. Jacob, M. Thamilselvan, D. Mangalaraj, S.K. Narayandass, J. Yi, Polym. Int. 53 (2004) 898–902.
[40] H.Y. Chen, P.P. Yu, Z.Z. Zhang, F. Teng, L.X. Zheng, K. Hu, X.S. Fang, Small 12 (2016) 5809–5816.
[41] Y.F. Wang, L. Li, H.B. Wang, L.X. Su, H.Y. Chen, W.P. Bian, J.G. Ma, B.S. Li, Z.G. Liu, A.D. Shen, Nanoscale 12 (2020) 1406–1413.
[42] C. Tusche, H.L. Meyerheim, J. Kirschner, Phys. Rev. Lett. 99 (2007) 026102.
[43] L.X. Wang, F.S. Wang, Chin. J. Appl. Chem. 7 (1990) 1–10.
[44] J. Cai, X.J. Xu, L.X. Su, W. Yang, H.Y. Chen, Y. Zhang, X.S. Fang, Adv. Opt. Mater. 6 (2018) 1800213.
[45] B. Zhao, F. Wang, H.Y. Chen, Y.P. Wang, M.M. Jiang, X.S. Fang, D.X. Zhao, Nano Lett 15 (2015) 3988–3993.
[46] S.M. Sze, Kwok K. Ng, in: Physics of Semiconductor Devices, John Wiley & Sons, 2006, pp. 91–92. third ed..
[47] J.T. Li, C.X. Xu, H.Y. Nan, M.M. Jiang, G.Y. Gao, Y. Lin, J. Dai, G.Y. Zhu, Z.H. Ni, S.F. Wang, Y. Li, ACS Appl. Mater. Interfaces 6 (2014) 10469–10475.
[48] S.X. Yang, J. Gong, Y.L. Deng, J. Mater. Chem. 22 (2012) 13899–13902.
[49] Y. Wang, L. Li, H. Wang, L. Su, H. Chen, W. Bian, J. Ma, B. Li, Z. Liu, A. Shen, Nanoscale 12 (2020) 1406–1413.
[50] P.P. Yu, K. Hu, H.Y. Chen, L.X. Zheng, X.S. Fang, Adv. Funct. Mater. 27 (2017) 1703166.
[51] W.B. Peng, X.F. Wang, R.M. Yu, Y.J. Dai, H.Y. Zou, A.C. Wang, Y.N. He, Z.L. Wang, Adv. Mater. 29 (2017) 1606698.
[52] O. Game, U. Singh, T. Kumari, A. Banpurkar, S. Ogale, Nanoscale 6 (2014) 503–513.